

Microlensing of Relativistic Knots in the Quasar HE1104–1805

Paul L. Schechter^{1,2}, A. Udalski³, M. Szymański³, M. Kubiak³, G. Pietrzyński^{3,4},
I. Soszyński³, P. Woźniak⁵, K. Żebruń³, O. Szewczyk³, and Ł. Wyrzykowski³

ABSTRACT

We present 3 years of photometry of the “Double Hamburger” lensed quasar, HE1104–1805, obtained on 102 separate nights using the OGLE 1.3-m telescope. Both the A and B images show variations, but with substantial differences in the lightcurves at all time delays. At the 310^d delay reported by Wisotzki and collaborators the difference lightcurve has an rms amplitude of 0.060 mag. The structure functions for the A and B images are quite different, with image A more than twice as variable as image B (a factor of 4 in structure function) on timescales of less than a month. Adopting microlensing as a working hypothesis for the uncorrelated variability, the short timescale argues for the relativistic motion of one or more components of the source. We argue that the small amplitude of the fluctuations is due to the finite size of the source with respect to the microlenses.

Subject headings: gravitational lenses; microlensing

1. INTRODUCTION

Two very different physical processes contribute to the observed photometric variability of gravitationally lensed quasars: the intrinsic variability of the quasar itself and propagation effects along the line of sight. Chief among the latter is microlensing by the stellar mass objects in the intervening lens (Chang and Refsdal 1979; Paczyński 1986). The combination of intrinsic and microlensing variations represents an embarrassment of riches. For the purpose of measuring lens time delays (using the correlated intrinsic variability of the quasar images) uncorrelated microlensing variations are an additional source of noise. Conversely, the intrinsic variation of the quasar pro-

duces correlated noise in the uncorrelated microlensing signals.

Time delays have been measured for nearly a dozen systems, and in most cases microlensing appears not to have presented a serious problem (e.g. Kundić et al. 1997; Schechter et al. 1997). Dramatic microlensing variations have been observed in the system 2237+0305 (Corrigan et al. 1991; Woźniak et al. 2000) but on a timescale (months) which is very much longer than the predicted delays (hours).

There have, however, been instances in which microlensing and time delay measurements have interfered with each other. In the case of 0957+561, the two images have long timescale (1000^d) variations (Refsdal et al. 2000), which bias the inferred time delay. Burud et al. (2000) report uncorrelated variations over timescales of several months in their study of B1600+434. Examination of their Figure 3 shows apparent uncorrelated variations on timescales of days. Uncorrelated variations are also reported by Hjorth et al. (2002) in their study of RXJ0911+0551.

We report here the results of an unsuccessful program to measure the time delay of the doubly imaged quasar HE1104–1805 (Wisotzki et al.

¹Massachusetts Institute of Technology, Cambridge, MA 02139-4307, USA schech@achernar.mit.edu

²Institute for Advanced Study, Princeton, NJ 08540-0631, USA

³Warsaw University Observatory, Al. Ujazdowskie 4, 00-478 Warszawa, Poland ([@astrouw.edu.pl](mailto:udalski,msz,mk,pietrzyn,soszynsk,zebrun,szewczyk,wyrzykow))

⁴Universidad de Concepción, Departamento de Física Casilla, 160-C, Concepción, Chile pietrzyn@hubble.cfm.udec.cl

⁵Los Alamos National Laboratory, MS-D436, Los Alamos, NM 87545, USA wozniak@lanl.gov

1993). In three years' monitoring with the Optical Gravitational Lensing Experiment (OGLE) 1.3m telescope at Las Campanas we see uncorrelated variations in the A and B images, which we interpret as the result of microlensing.

In §2 we describe the observations and initial reductions. In §3 we compare light curves for the two quasar images, A and B, using the time tested chi-by-eye technique and a less subjective method. Our data fail to produce a satisfactory time delay. In §4 we derive structure functions separately for the A and B images. Adopting the time delay measured by Gil-Merino et al. (2002), we determine a structure function for the microlensing from the difference between the A and B images. In §5 we explore several alternative interpretations of the structure functions for the two quasar images.

2. OBSERVATIONS

Observations of HE1104–1805 were carried over a three year period as a sub-project of the second phase of the OGLE microlensing search (Udalski, Kubiak and Szymański 1997). The 1.3-m Warsaw telescope at the Las Campanas Observatory, Chile (operated by the Carnegie Institution of Washington) was equipped with the “first generation” camera, incorporating a SITE 2048 × 2048 CCD detector working in still-frame mode. The pixel size was 24 μm , giving a scale of 0''.417/pixel. Observations were performed in the “medium” readout mode of the CCD detector, with a gain 7.1 e^-/ADU and read noise of about 6.3 e^- . Details of the instrumentation setup can be found in Udalski, Kubiak and Szymański (1997).

Our plan was to obtain data three times per month, at moon phase -11 , -1 and $+8$ days, weather permitting. If not, data was obtained on the first good night following the planned observation. Typically two 10 minute exposures were taken with a standard V-band filter. The data were reduced automatically at the telescope using the OGLE software pipeline. Photometry of the two quasar components, A and B, and for three reference stars, CA, CB and CC was derived with the DoPHOT photometry program (Schechter, Mateo and Saha 1993). The third of these reference stars proved to be variable. Stars CA and CB are $-3''.2$ and $31''.9$ to the East and

$15''.1$ and $5''.3$ to the South, respectively from the brighter quasar component, A. All magnitudes are referred to the average of these two stars. No attempt was made to correct either for color terms or for an airmass/color crossterm. Figure 1 presents a $120'' \times 120''$ subraster of a V-band frame of HE1104–1805 showing both quasar images, A and B, and both reference stars, CA and CB.

The complete record of observations is given in Table 1. Three exposures which gave very different magnitudes from the exposure immediately preceding or following and from magnitudes obtained earlier or later in the month are flagged and are not used in the discussion that follows. Data taken on the same night was averaged and was assigned the average time of observation. Nightly averaged photometry for quasar images A and B and for comparison star CA is shown in Figure 2. Note that there is no additional information in star CB, as its variations mirror those of CA, but with the opposite sign. We do not plot formal error bars, as night-to-night variations are always larger than these.

3. TIME DELAY

Wisotzki and collaborators (Wisotzki et al. 1998; Gil-Merino et al. 2002) have measured a time delay of $310 \pm 19^{\text{d}}$ for HE1104–1805, with the B image leading the A image. In Figure 3 we plot our photometry (averaged over each night, typically two exposures) for image B at the corresponding time for image A, 310^{d} later than actually observed. The photometry for image A is shown as actually observed.

3.1. Difference Lightcurve

As we are looking at a single quasar along lines of sight that differ by only a few arcseconds, the intrinsic component of the A and B variability ought to be the same after compensation for the time delay. A lagged difference lightcurve should show only the effects of extrinsic processes, e.g. microlensing. The price we pay in so doing is that the difference lightcurve includes extrinsic variations (and noise) from both images.

In computing a lagged difference, we chose to interpolate on the B lightcurve, which is considerably smoother. Our approach was to use all data taken within 20 days of the desired time. We fit

a straight line (quadratic) if the desired time was straddled by two (three or more) observations; if not we took a straight average.

Figure 3 shows a difference lightcurve, obtained by interpolating on image B as described above. While there are modest similarities in the two lightcurves, the differences are substantial.

It should be noted that our single initial observation of image B in August 1997 (HJD 2450666) yields 5 points at the extreme left of the difference curve. We choose to keep these points because of the extra baseline they gain us. The advisability of this rests heavily on the assumption that B varies slowly.

3.2. Time Delay

Over the course of the three years spent observing HE1104–1805, with the acquisition of every new data point, we attempted to determine a time delay using the time honored “chi-by-eye” approach. At no point were we able to persuade ourselves that we had a robust determination of the time delay. In particular there are many significant features in the A lightcurve for which the B lightcurve has no counterpart. A variety of sophisticated techniques have been developed to extract time delays (see Gil-Merino et al. 2002 and references cited therein), but should one believe a time delay that fails the chi-by-eye technique?

We subscribe to Lord Rutherford’s dictum (Bailey 1967) – “If your experiment needs statistics, you ought to have done a better experiment.” But since the community standard would seem to be that one must carry out an “objective” test, we have done so. As the B image seems to vary less than the A image, we interpolate over the B values as described above to obtain a prediction for A at a trial value of the time delay. We then compute the rms deviation between the observed magnitude for a wide range of time delays, plotted in Figure 4. The rms scatter at the published time delay is 0.060 mag, with 51 overlapping points. There is a minimum of 0.054 at 145^d with 56 overlapping points. Without knowing the statistics of the uncorrelated features we cannot argue whether either of these is to be preferred over yet some other value.

We admit defeat. We cannot measure the time delay using our data and, for the purpose of the

ensuing discussion, we use the value of Gil-Merino et al. If the variations intrinsic to HE1104–1805 were large, the error in our adopted delay would introduce a spurious microlensing signal. But had the intrinsic variations been large, we would have been able to measure the delay.

4. VARIABILITY IN THE A AND B IMAGES

4.1. Structure Functions for A and B

It is our subjective impression that the A lightcurve in Figure 2 is much more variable than the B lightcurve. This can be made quantitative by computing structure functions for images A and B,

$$s(\tau) = \left\langle [(m(t + \tau) - m(t))^2] \right\rangle, \quad (1)$$

where angle brackets denote an average over time. Figure 5 shows these functions computed for images A and B, in 9 day bins. As in the previous section we use the nightly averages to compute individual values of $m(t)$. The first bin includes lags $0 < \tau < 4^{\text{d}}5$, the second lags $4.5 < \tau < 13^{\text{d}}5$, and so forth. The structure function for image A shows considerably more variability than that for image B. For lags shorter than 40 days it is a factor of four larger, corresponding to a factor of two more variability. We compute structure functions for the difference between comparison stars A and B, and find a roughly constant amplitude of 0.0002, corresponding to photometric errors of 0.014 mag. If measurement errors make a similar contribution to image B, the structure function for image A at 9 days is a factor of eight larger than for B.

4.2. Working Hypotheses

The A image is brighter than the B image, but not so bright that the images are anywhere near saturation. We can think of no reason why the measurement errors for A should be larger than for B. As we have made no attempt to account for the difference in color between the comparison stars and the quasar images, one might expect photometric errors to show a seasonal correlation (and hence an increasing structure function) depending upon whether the object was observed at low or high airmass. But the variations seen in both the A and B images are so large that we take

them to be the result of physical processes beyond the Earth’s atmosphere.

We take the difference in the amplitudes of the two structure functions to be significant, indicating that whatever physical processes are at work, they affect the images differently. Were we working at radio wavelengths, scintillation arising in the intervening galaxy would need to be considered, as it was by Koopmans and de Bruyn (2000) in the case of B1600+434. For lack of a better explanation (and perhaps a lack of imagination), we adopt, as our working hypothesis, that the fluctuations in image A are due largely to microlensing by stars in the lensing galaxy.

Some variation is expected due to the intrinsic variability of the quasar. The structure functions for quasars typically have amplitudes of $(0.1 \text{ mag})^2$, with time constants of order one year (Cristiani et al. 1996). There are, of course, very substantial variations among quasars, with some showing almost no variability and others showing intraday variability. The lightcurves and structure functions for A and B look so different that we take the variations in image B to be largely intrinsic, consistent with our expectations for typical quasars. A smaller microlensing amplitude might naively be expected because the surface brightness of the lensing galaxy is much lower at the position of image B and because we expect a continuous dark matter component to be a larger fraction of the mass. While the effects of dark matter are not quite so simple (Schechter and Wambsganss 2002; see below), it is nonetheless the case that microlensing should indeed affect A more than B.

4.3. Difference Structure Function

Figure 6 shows the structure function obtained for the difference lightcurve presented in Figure 3. We take its large fluctuations to be the accidental beating of features in lightcurve A against features in lightcurve B. For the purpose of comparison with microlensing simulations, we will want a characteristic timescale for the difference lightcurve. While the curve is exceedingly noisy, we estimate the time for our structure function to rise to one quarter of its asymptotic value, $T_{1/4}$, to be $\sim 20^d$.

5. INTERPRETATION

5.1. Microlensing at High Optical Depth

High optical depth microlensing differs qualitatively from its low optical depth counterpart. A great many microimages contribute to the observed flux of macroimages like A and B in HE1104-1805 (Paczynski 1986). Their combined flux may be efficiently simulated by tracing rays back from the observer to the source plane (Kayser et al. 1986; Wambsganss 1992; Lewis and Irwin 1995), producing a magnification map. As a source moves with respect to the lensing galaxy, it cuts across this magnification map, producing a simulated lightcurve.

At low optical depth such lightcurves have long, relatively constant intervals, punctuated by occasional large fluctuations. At high optical depth the lightcurves are more uniform in time, but there are still large amplitude “events” caused by the creation and annihilation of pairs of microimages as the source crosses “caustics,” and by close encounters with “cusps” in the magnification map. To first order the structure functions for such simulated lightcurves have a rise time whose scale is governed by the size the Einstein rings of the microlenses and whose amplitude depends upon the surface density of microlenses and the local shear (Lewis and Irwin 1995; 1996).

A minimum of three parameters is needed to characterize the microlensing of a macroimage: a dimensionless surface density of microlenses, κ_* , a dimensionless surface density of a smooth “dark” component, κ_c , and a dimensionless tidal stretching or shear, γ . For a multiply imaged quasar, the image positions (and sometimes magnifications) give a model that constrains γ and $\kappa_{tot} \equiv \kappa_c + \kappa_*$ at the position of each image. Paczyński (1986) shows that the relevant model space collapses to an equivalent two dimensional space spanned by an effective dimensionless surface density, $\kappa_*^{eff} = \kappa_*/(1 - \kappa_c)$ and an effective shear, $\gamma^{eff} = \gamma/(1 - \kappa_c)$, but with the magnifications larger by $1/(1 - \kappa_c)^2$ than those computed from the effective values.

The amplitudes of the microlensing fluctuations go to zero in the limits both of unit magnification (no microlenses) and in the case very high magnification (when fluctuations in the number of

microimages become negligible). Taking the effective magnification to be given by $\mu^{eff} = 1/[(1 - \kappa_*^{eff})^2 - (\gamma^{eff})^2]$, the largest microlensing fluctuations occur when $\mu^{eff} \sim 3$ (Granot et al. 2002). Macroimages that are saddlepoints of the arrival time surface (those with $1 - \kappa - \gamma < 0$) show larger fluctuations than those that are minima. The fluctuation amplitudes for minima appear to peak at roughly one magnitude, but those for saddlepoints can be somewhat larger (Schechter and Wambsganss 2002). The magnification histograms for both minima and maxima are bimodal in the vicinity of $\mu^{eff} \sim 3$. A histogram computed from the observed difference lightcurve for HE1104-1805 is shown in Figure 7.

5.2. Macromodel for HE1104–1805

We have used the Lehár et al. (2000) HST positions for the components of HE1104–1805 and the lensing galaxy, and an emission line flux ratio $A/B = 2.8$ (Wisotzki 1993) to model the lensing potential as a singular isothermal sphere in the presence of external shear. The dimensionless surface density, shear and magnification for the A and B images are given in Table 2, with negative magnification indicating a saddlepoint. The shear is sufficiently large in this system that it seems unlikely to be the result of flattening of the lensing potential. Fitting models which had steeper (shallower) potentials would give lower (higher) surface densities and lower (higher) magnifications, but for reasonable ranges the conclusions of the subsequent sections are essentially unchanged.

5.3. Fluctuation Amplitude: Image A

The structure function computed from a lightcurve (or its two dimensional counterpart, computed from a magnification map) will be characterized by a dimensionless amplitude and a time scale (or length scale). At large temporal (or spatial) separations, we expect the amplitude to saturate at some asymptotic value. The amplitude is governed by two dimensionless parameters: the ratio of the size of the source to the size of a microlens (its Einstein ring radius), and the fraction of the total surface density in microlenses, as opposed to a smoothly distributed component. The time scale is set by dividing the size of the Einstein ring by the velocity of the source relative to the

microlenses.

The size of the Einstein ring clearly affects both the fluctuation amplitude and the timescale. Here we adopt an idealized model which makes it particularly easy to separate the effects of source size from those of dilution by smoothly distributed matter. We take the source to have two components, one very much smaller than the microlenses and one very much bigger. In such a scenario, the amplitude of the fluctuations is smaller by the ratio of the flux in the smaller component to the total flux. We draw tentative conclusions using this model and then consider how relaxing our assumptions might affect them.

5.3.1. Dark Matter Dilution

The observed distribution for the shifted magnitude differences between the A and B images of HE1104–1805 has an rms scatter of 0.060 magnitudes. Our working hypothesis is that these result from microlensing fluctuations in image A. Lewis and Irwin (1995, 1996) present microlensing results for a point source with $(\kappa_*, \gamma) = (0.65, 0.50)$ – approximately correct for image A if $\kappa_*/\kappa_{tot} = 1$. They predict fluctuations of order 1 magnitude. An extended source would give smaller fluctuations. Alternatively, one might suppose that increasing the smooth component, κ_c , at the expense of the microlensing component, κ_* , would likewise produce smaller fluctuations.

We therefore prevailed upon J. Wambsganss to carry out a series of microlensing simulations for $(\kappa_{tot}, \gamma) = (0.60, 0.50)$, decreasing κ_*/κ_{tot} from 1 to 0. We were flabbergasted to discover that the fluctuations increased rather than decreased, at least at first (Schechter and Wambsganss 2002). Eventually the fluctuations get small, but only when $\kappa_*/\kappa_{tot} \ll 1$. At such levels of dilution, the magnification histogram is exceedingly asymmetric, with a relatively narrow spike at the expected magnification and a tail roughly 2 magnitudes long toward large demagnifications. This is not the character of the fluctuations observed in Figure 7. Moreover this would require an extraordinarily low mass-to-light ratio for the stellar component of the lensing galaxy. We conclude that a model in which the small observed fluctuations are due to dilution by dark matter is not viable.

But we *do* expect some dark matter dilution.

In their study of the lensing galaxy in the system 0047–281, Koopmans and Treu (2002) find the stellar mass fraction interior to the Einstein ring to be 0.58 ± 0.04 . It seems reasonable to take it to be a factor of ~ 2 smaller at the Einstein ring. If HE1104–1805 were similar, it would imply $(\kappa_*/\kappa_{tot})_A = 0.35$.

5.3.2. A Source with a Big and a Small Component

For our idealized model, the fluctuations are diluted by the ratio of the flux in the compact component to the total flux. In Wambsganss’ simulations the rms fluctuations vary from 0.69 mag for $\kappa_*/\kappa_{tot} = 1$ through 1.21 mag for $\kappa_*/\kappa_{tot} = 0.16$, beyond which the fluctuations begin to decrease. At $\kappa_*/\kappa_{tot} = 0.35$ the rms fluctuations are about 1 magnitude. A microlensed hot spot would therefore need $\sim 7\%$ of the total flux to produce the observed lensing histogram.

Interestingly, the magnification histograms for $0.15 < \kappa_*/\kappa_{tot} < 0.50$ bifurcate into two peaks, separated by roughly 1.6 magnitudes (cf. Figure 3 of Schechter and Wambsganss 2002). A hotspot with 7% of the total flux would produce two fluctuation peaks separated by 0.10 mag. Aided by theory, one can imagine such a bifurcation in the observed histogram for HE1104–1805, Figure 7.

5.4. Fluctuation Amplitude: Image B

Figure 5 shows considerably less fluctuation in image B than in image A. This might be expected both because the stellar surface density is lower at B than at A, and because the dark matter fraction is higher at B. Substituting dark matter for microlenses might increase the microlensing fluctuation for high magnification images, especially saddlepoints, but it does not for lower magnification minima.

Our isothermal model gives us the total surface density at A and B, with $\kappa_{tot,B}/\kappa_{tot,A} = 0.52$. Lehar et al. (2000) measure the effective radius for the lensing galaxy, $r_e = 0''.73$. Images A and B are $1''.10$ and $2''.12$, respectively, from the lensing galaxy. For constant M/L we then have $\kappa_{*,B}/\kappa_{*,A} = 0.22$. We therefore expect $(\kappa_*/\kappa_{tot})_B = 0.42(\kappa_*/\kappa_{tot})_A$.

If we take $(\kappa_*/\kappa_{tot})_A = 1$, we get $\kappa_{*,B} = 0.140$ and $\kappa_{c,B} = 0.204$. These give $\kappa_*^{eff} = 0.176$

and $\gamma^{eff} = 0.263$. Under these circumstances, we would expect, according to Lewis and Irwin (1996), microlensing fluctuations in image B to be roughly half as large as in image A, which is marginally consistent with the structure functions of Figure 5, though perhaps not at the shortest lags.

If we take $(\kappa_*/\kappa_{tot})_A = 0.35$, the fluctuations for image A increase and the fluctuations for image B decrease. In this case most of the fluctuation in image B would be due to intrinsic variations in the quasar.

In any event, the character of the microlensing light curve predicted for B is quite different than that predicted for A. At the lower surface density of image B we expect infrequent but high magnification events (and pairs of events), with the spacing between events large compared to their rise times and durations. Substituting dark matter for microlenses makes such events yet more infrequent. We may not have sampled image B long enough to see any of its occasional fluctuations.

5.5. Tentative Conclusions

While the small amplitude of the fluctuations is primarily due to finite source size effects, the above arguments would seem to favor some dilution of the stellar component with dark matter at both A and B for the following reasons: a) it minimizes the flux of the hotspot b) it reduces the predicted amplitude of microlensing fluctuations in image B and c) it produces a bimodal magnification histogram for image A.

5.6. Timescale

To first approximation, simulated microlensing structure functions look like the voltage across the capacitor in an RC circuit, rising and then asymptotically approaching a constant value. Lewis and Irwin (1996) add an additional parameter that allows for more protracted rises, but for the present discussion it suffices to think in terms of their $T_{1/2}$, the time it takes for their structure function to reach half its asymptotic value. Lewis and Irwin use a variant of the structure function which computes the sum of absolute values of differences rather than the sum of squares in equation (1), so their $T_{1/2}$ corresponds roughly to our $T_{1/4}$. For a range of cases with $\kappa_* = \gamma$ and no

smooth component (as would be appropriate for a singular isothermal sphere), they find $T_{1/2} \sim 0.33$, (measured in Einstein ring radii per unit time) for source trajectories that cross the shear direction at a 45° angle to the shear.

The radius of the Einstein ring, projected back onto the source plane, is given by

$$R_E = \left[\frac{4GM}{c^2} \frac{D_{LS}D_S}{D_L} \right]^{\frac{1}{2}} \quad (2)$$

where D_L , D_S , D_{LS} and are angular diameter distances to the lens, the source and from the lens to the source, respectively. The redshifts for the lens and quasar are 0.729 and 2.319, respectively (Lidman et al. 2000), giving $D_L H_0/c = 0.350$, $D_S H_0/c = 0.395$ and $D_{LS} H_0/c = 0.212$ for $(\Omega_m, \Omega_\Lambda) = (0.3, 0.7)$. We therefore have

$$R_E = 4.31 \times 10^{16} \text{cm} \left(\frac{M}{M_\odot} \right)^{\frac{1}{2}} \left(\frac{70 \text{km/s/Mpc}}{H_0} \right)^{\frac{1}{2}} \quad \text{and} \quad (3)$$

$$T_{1/2} \sim 5^{\text{d}} 55 \left(\frac{c}{v} \right) \left(\frac{M}{M_\odot} \right)^{\frac{1}{2}} \left(\frac{70 \text{km/s/Mpc}}{H_0} \right)^{\frac{1}{2}}, \quad (4)$$

where our decision to normalize the source velocity by the speed of light reflects the remarkably short timescale for the observed fluctuations. Our observed $T_{1/4} \sim 20^{\text{d}}$ timescale implies a source velocity of $\sim 0.25c$ for solar mass microlenses.

5.7. Alternative Models and Interpretations

5.7.1. Intermediate Sized Optical Continuum

Our working model takes the source to have two components, one very much smaller than the microlenses and one very much bigger. The range of possible alternative models for the surface brightness distribution of the source is limited only by imagination. Source models favored in the microlensing literature include Gaussians and uniform disks as well as more physically motivated models (Agol and Krolik 1999). In the case of HE1104–1805, source velocities approaching the speed of light are indicated. It seems unlikely that the entire optical continuum region would be move, as a unit, with such a velocity.

There is evidence, however, that the continuum source cannot be too much larger than the mi-

cro-lenses. In their discovery paper, Wisotzki et al. (1993) note that while the emission line flux ratio is constant at a factor of 2.8, the continuum flux ratio increases to the blue, rising to a factor ~ 6 in the B filter. They argue that the continuum source is likely to be more compact than the broad line region, and that the continuum is microlensed. In this case we would be underestimating, by roughly a factor of 2, the fractional contribution of the fast moving region to the unlensed flux.

5.7.2. Nanolensing by $10^{-5} M_\odot$ Planets

An alternative explanation that would obviate the need for relativistic velocities invokes microlenses with planetary masses, of order $10^{-5} M_\odot$ (Schild 1996 and references cited therein). The velocity of the source relative to the lensing system would then be of order $10^{-3}c$. Such “nanolenses” impose correspondingly tighter constraints on the size of the compact part of the source. Wyithe and Loeb (2002) therefore argue that hotspots are still needed in such a model: the accretion disk would be larger than the nanolenses but the hotspots might be smaller.

An additional difficulty associated with this hypothesis is that microlensing by stars might interfere with nanolensing. The anomalously large fluctuations found by Schechter and Wambsganss (2002) depend critically on the lensing potential being smooth on larger scales. If the macro-image is broken up into micro-images, nanolenses will operate separately on each of these to smaller effect.

5.7.3. Coldspots

Wyithe and Loeb (2002) argue that short timescale fluctuations observed by Hjorth et al. (2002) and Burud et al. (2002) might be due the microlensing of broad absorption line clouds shadowing a quasar accretion disk. None of the figures they present for these models look much like our data: either the amplitudes are too small or the timescales are too long.

5.7.4. Multiple Hotspots

Interestingly, Wyithe and Loeb also simulate hotspots that arise within the quasar’s accretion disk, as proposed by Gould and Miralda-Escudé (1997). These have orbital velocities $\sim 0.2c$. Their model with only a single hotspot shows a strong

periodicity and the classic M-shaped profile associated with the creation and annihilation of a single pair of micro-images. While we see no such a periodic signal in our data, it would be premature to rule out a single, accretion disk hotspot on the basis of a single set of model parameters. A relativistic hotspot in a jet would likewise not be excluded by their model.

Interestingly, the lightcurve for their model with 100 hotspots shows considerably more resemblance to the difference lightcurve for HE1104–1805, both in amplitude and scale. Moreover their parameters, $\kappa_{tot} = \gamma = 0.54$ and $\kappa_* = 0.08$, are quite similar to those we adopt for the B image of HE1104–1805. They produce a saddlepoint with a magnification $\mu = -12.5$ and microlens fraction of 15%, almost ideal for the purpose of maximizing microlensing fluctuations.

6. SUMMARY

Three years of observations of the two lensed quasar images of HE1104–1805 show variations in the A and B images that are uncorrelated, with V amplitudes of ~ 0.060 mag. The A image exhibits considerably more variability, on a timescale $\lesssim 1$ month, while the fluctuations in the B image are consistent with our expectations for variations intrinsic to the quasar.

On the hypothesis that the fluctuations are due to microlensing by solar mass stars, the implied source velocity is $\sim 0.25c$. For reasonable assumptions regarding the ratio of dark to microlensing matter and on the assumption that only a single hotspot is contributing to the fluctuations, the hotspot contributes $\sim 7\%$ of the continuum flux. A multiple hotspot model presented (and rejected) by Wyithe and Loeb (2002) also seems viable, perhaps even preferable, in the present case.

We thank Professor B. Paczyński for his support and Professor J. Wambsganss for his counsel. We gratefully acknowledge the support of the US NSF through grants AST96-16866, AST98-20314 and AST02-06010. PLS thanks the John Simon Guggenheim Memorial Foundation its support and the Institute for Advanced Study for its hospitality.

REFERENCES

- Agol, E. & Krolik, J. 1999, *ApJ*, 524, 49
- Bailey, N. J. T. 1967, *The Mathematical Approach to Biology and Medicine* (New York: Wiley)
- Burud, I. et al. 2000, *ApJ*, 544, 117
- Burud, I. et al. 2002, *A&A*, 391, 481
- Chang, K. & Refsdal, S. 1979, *Nature*, 282, 561.
- Corrigan, R. T. et al. 1991, *AJ*, 102, 34
- Cristiani, S., Trentini, S., La Franca, F., Aretxaga, I., Andreani, P., Vio, R., & Gemmo, A. 1996, *A&A*, 306, 395
- Gil-Merino, R., Wisotzki, L., & Wambsganss, J. 2002, *A&A*, 381, 428
- Gould, A. & Miralda-Escude, J. 1997, *ApJ*, 483, L13
- Hjorth, J., et al. 2002, *ApJ*, 572, L11
- Kayser, R., Refsdal, S., & Stabell, R. 1986, *A&A*, 166, 36
- Koopmans, L. V. E. & de Bruyn, A. G. 2000, *A&A*, 358, 793
- Koopmans, L. V. E. & Treu, T. 2002, preprint (astro-ph/0205281)
- Kundic, T. et al. 1997, *ApJ*, 482, 75
- Lehár, J. et al. 2000, *ApJ*, 536, 584
- Lewis, G. F., Irwin, M. J. 1995, *MNRAS* 276, 103
- Lewis, G. F., Irwin, M. J. 1996, *MNRAS* 283, 225
- Lidman, C., Courbin, F., Kneib, J.-P., Golse, G., Castander, F., & Soucail, G. 2000, *A&A*, 364, L62
- Paczynski, B. 1986, *ApJ* 301, 503
- Rauch, K. P., Mao, S., Wambsganss, J., Paczyński, B. 1992, *ApJ* 386, 30
- Refsdal, S., Stabell, R., Pelt, J., & Schild, R. 2000, *A&A*, 360, 10
- Schechter, P. L., Mateo, M., & Saha, A. 1993, *PASP*, 105, 1342

- Schechter, P. L. et al. 1997, ApJ, 475, L85
- Schechter, P. L. & Wambsganss, J. 2002 preprint (astro-ph/0204425)
- Udalski, A., Kubiak, M., & Szymański, M. 1997, AcA, 47, 319
- Wambsganss, J. 1992, ApJ 386, 19
- Wambsganss, J., Witt, H. J., Schneider, P. 1992, A&A 258, 591
- Wisotzki, L., Köhler, T., Kayser, R., Reimers, D. 1993, A&A 278, L15
- Wisotzki, L., Wucknitz, O., Lopez, S., & Sorensen, A. N. 1998, A&A, 339, L73
- Witt, H. J. 1993, ApJ 403, 530
- Woźniak, P., Udalski, A., Szymański, M., Kubiak, M., Pietrzyński, G., Soszyński, I., & Żebruń, K. 2000, ApJ, 540, L65
- Wyithe, J. S. B. & Loeb, A. 2002, preprint (astro-ph/0204529)

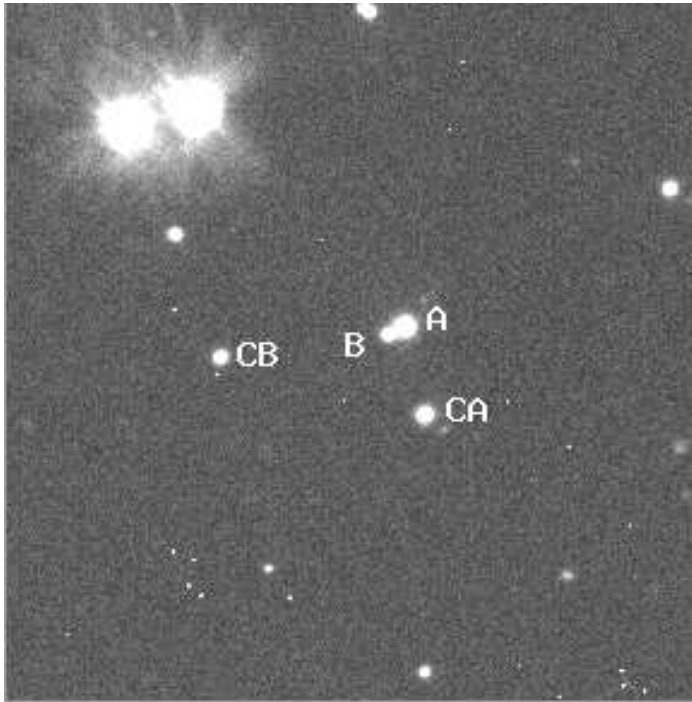


Fig. 1.— A $120'' \times 120''$ V filter direct image of HE1104–1805 showing QSO components A and B and comparison stars CA ($V = 17.65 \pm 0.02$) and CB ($V = 18.43 \pm 0.03$). North is up and East to the left.

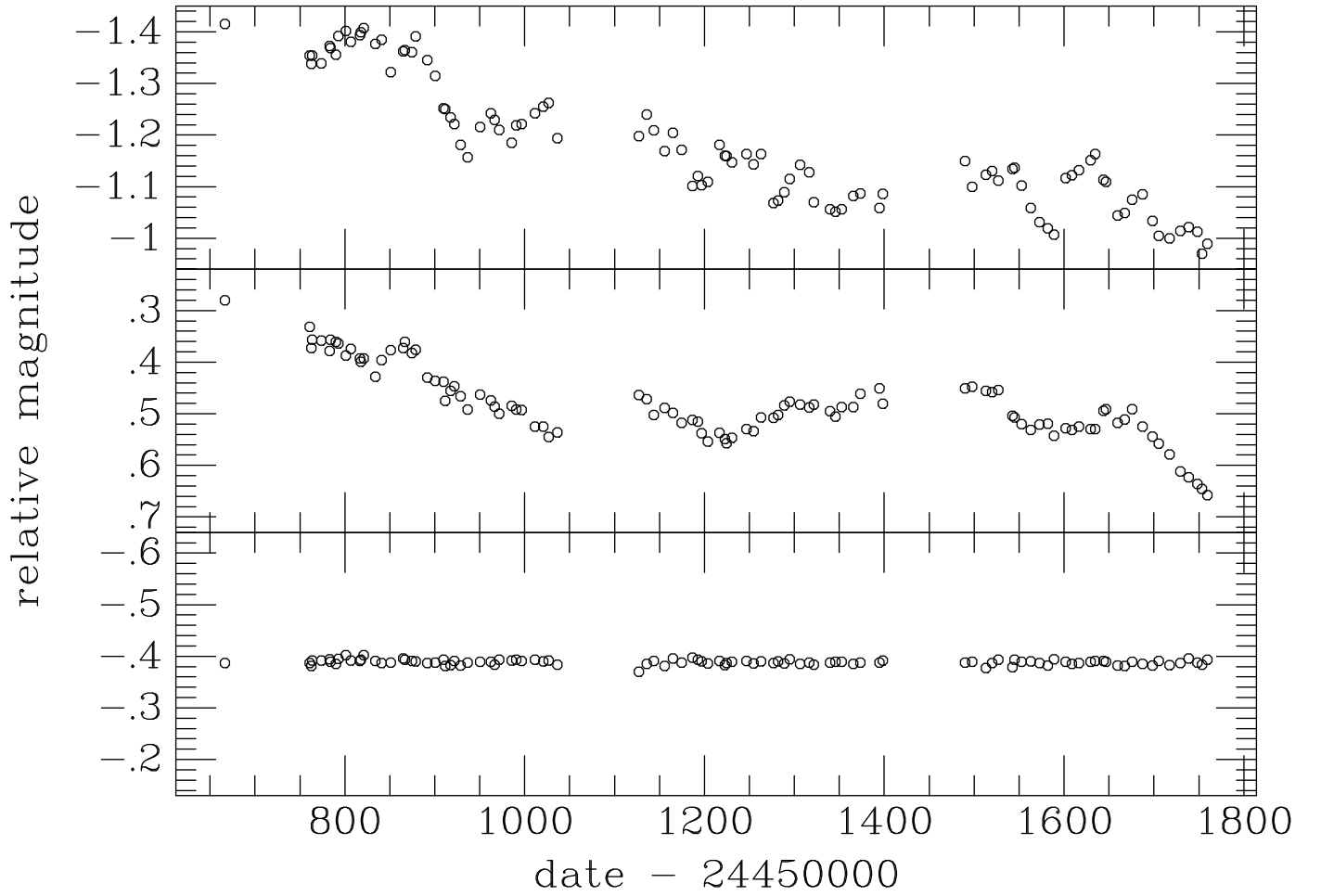


Fig. 2.— Lightcurves for QSO components *A* (top) and *B* (middle) and for comparison star *CA* (bottom).

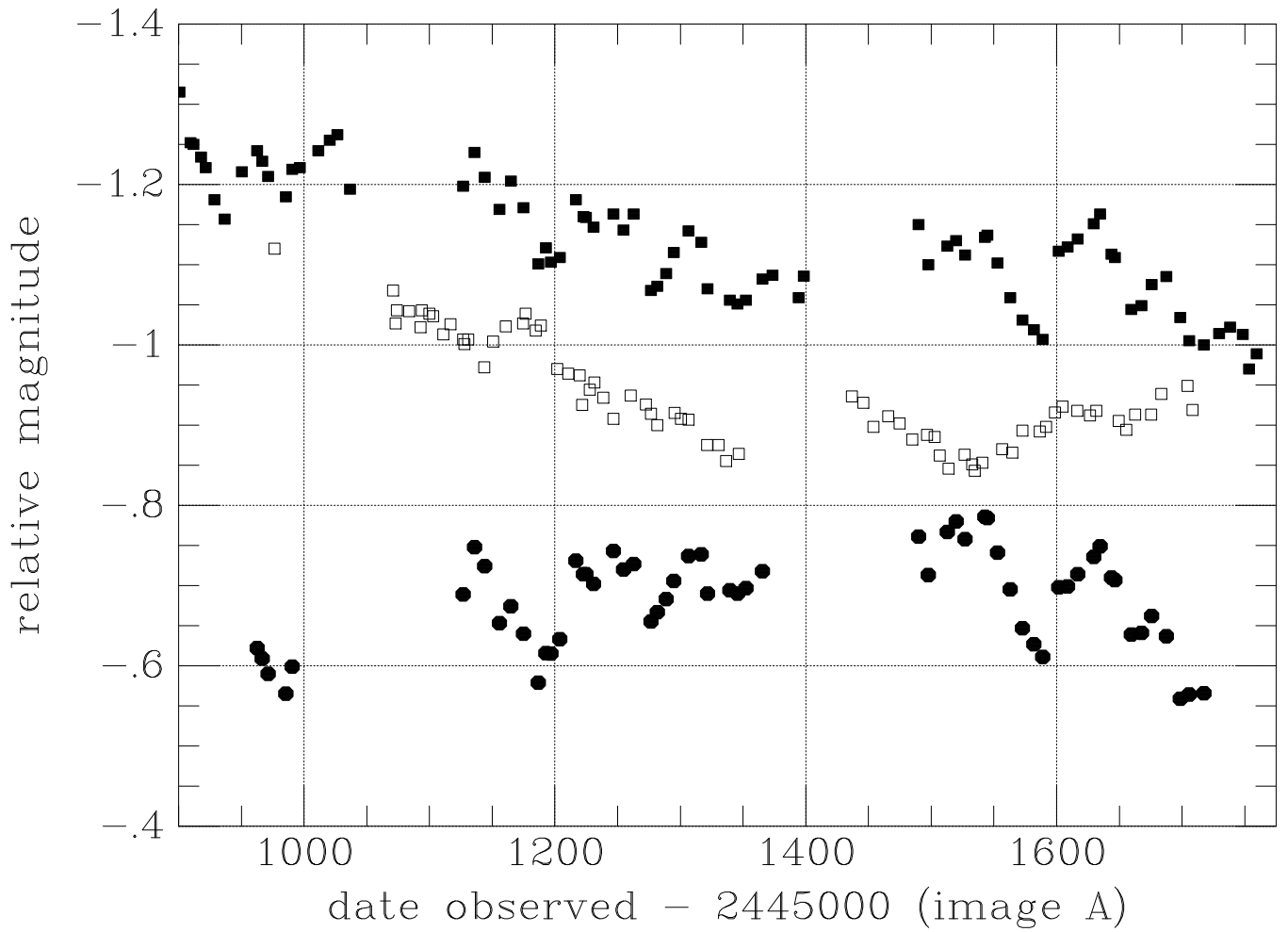


Fig. 3.— filled squares ■ – lightcurve for QSO component A; open squares □ – B lightcurve shifted horizontally 310 days to a later date and brighter by 1.4 mag; filled circles ● – the difference between the A lightcurve and interpolation on upon the shifted B lightcurve, shifted fainter by 0.9 mag.

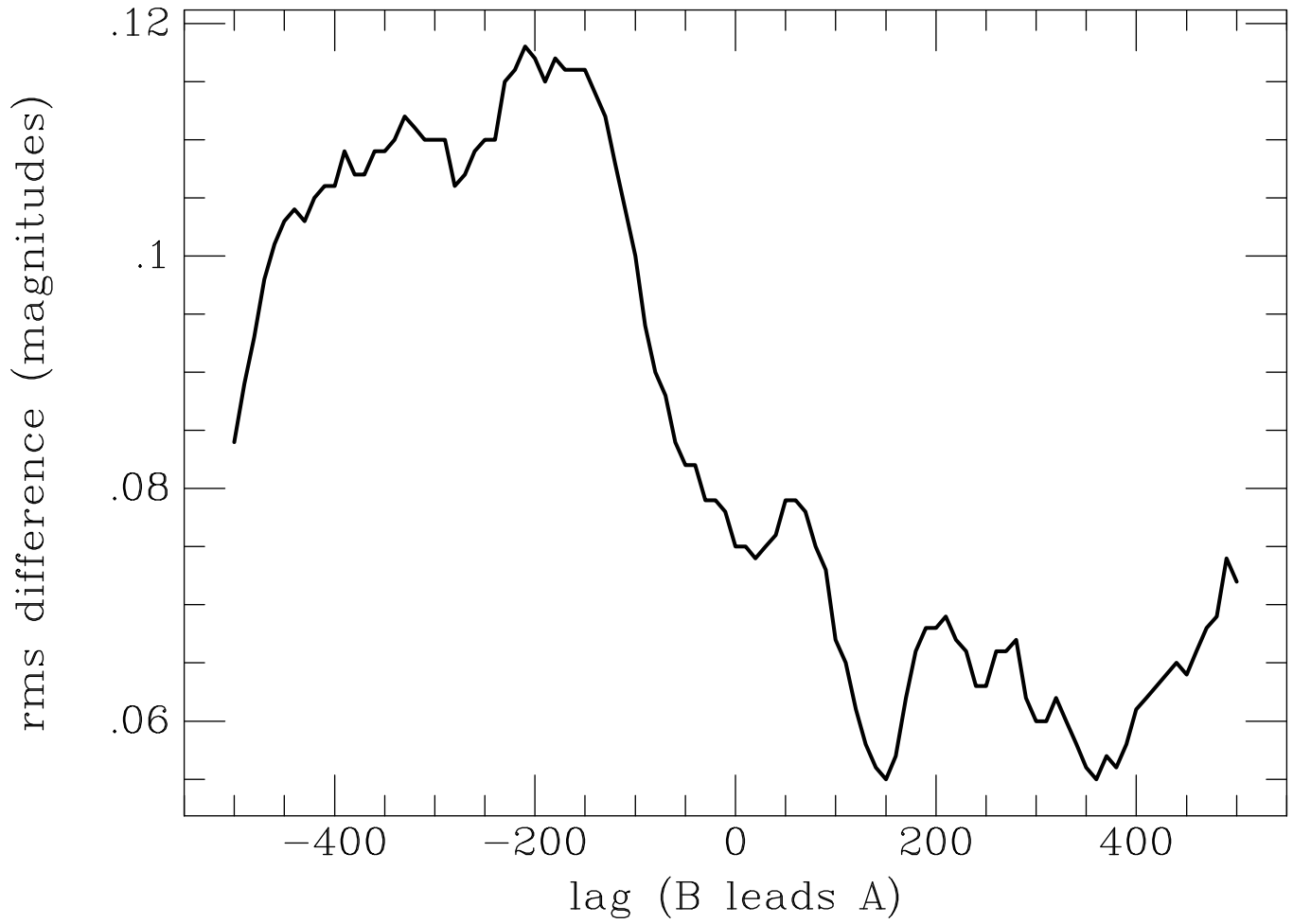


Fig. 4.— RMS difference between the observed lightcurve for QSO component *A* and interpolation on *B* lightcurve shifted to a later date.

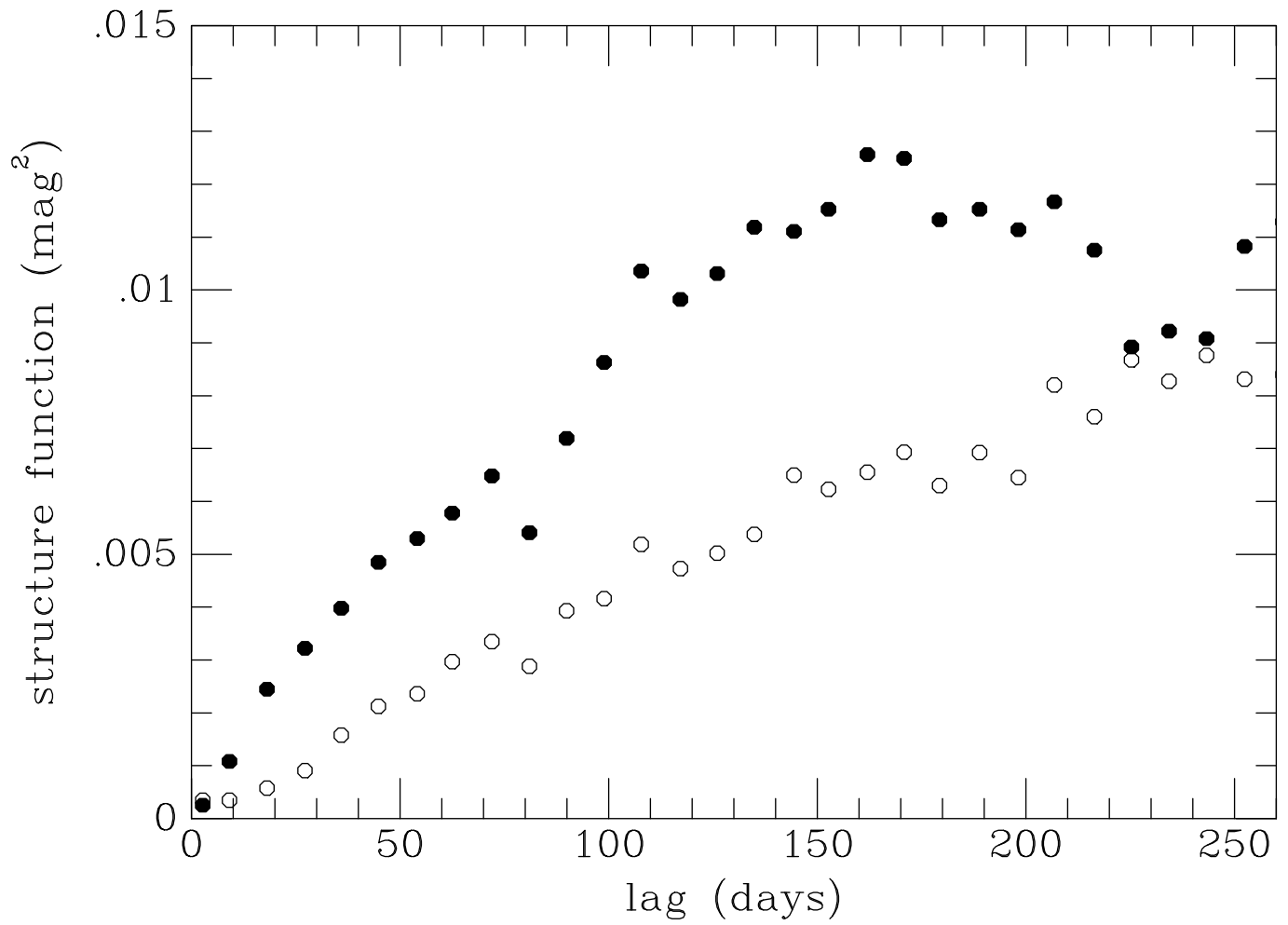


Fig. 5.— Structure functions for the *A* (●) and *B* (○) lightcurves binned in 9 day intervals.

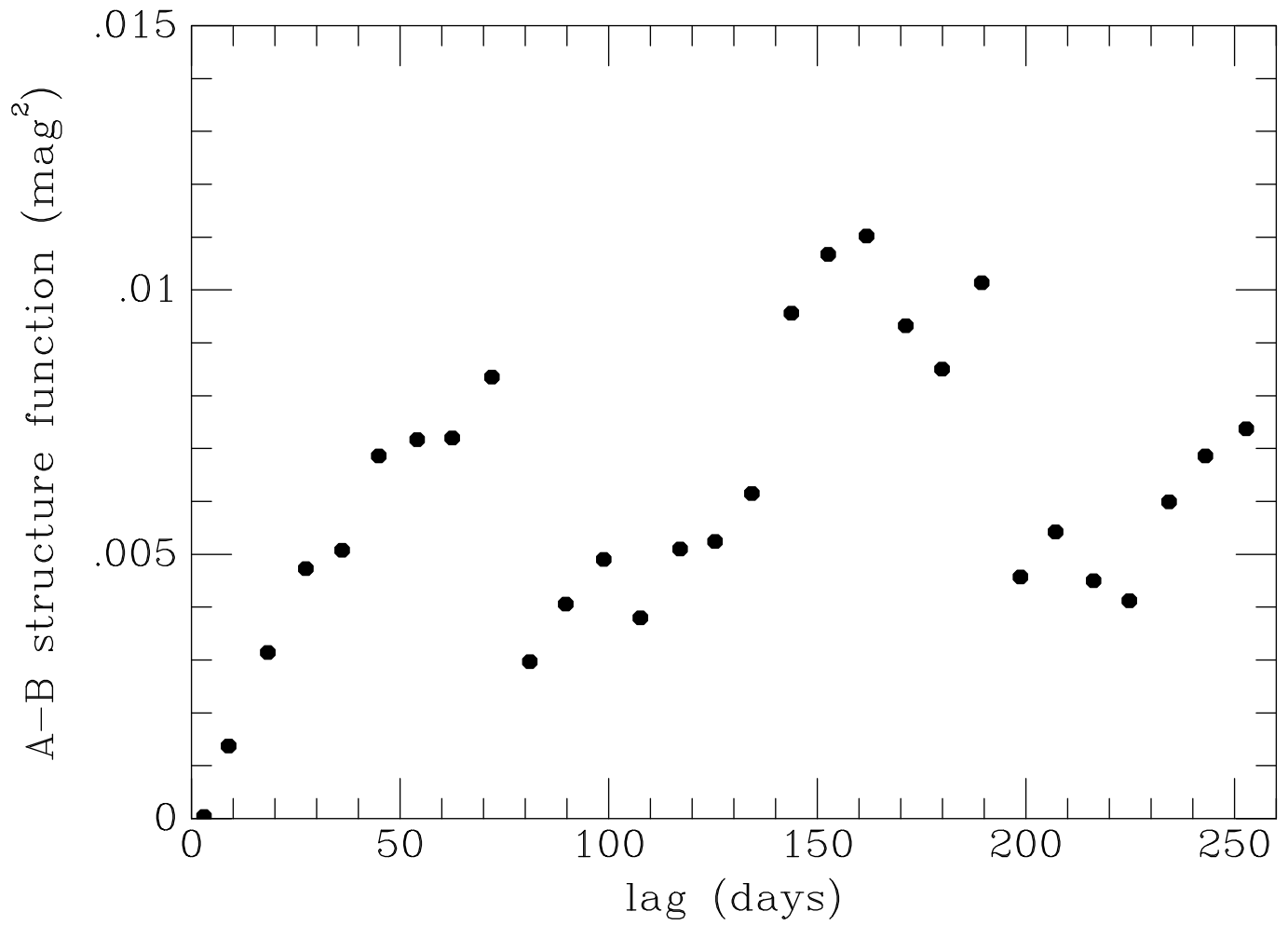


Fig. 6.— Structure function for the $A - B$ difference lightcurve.

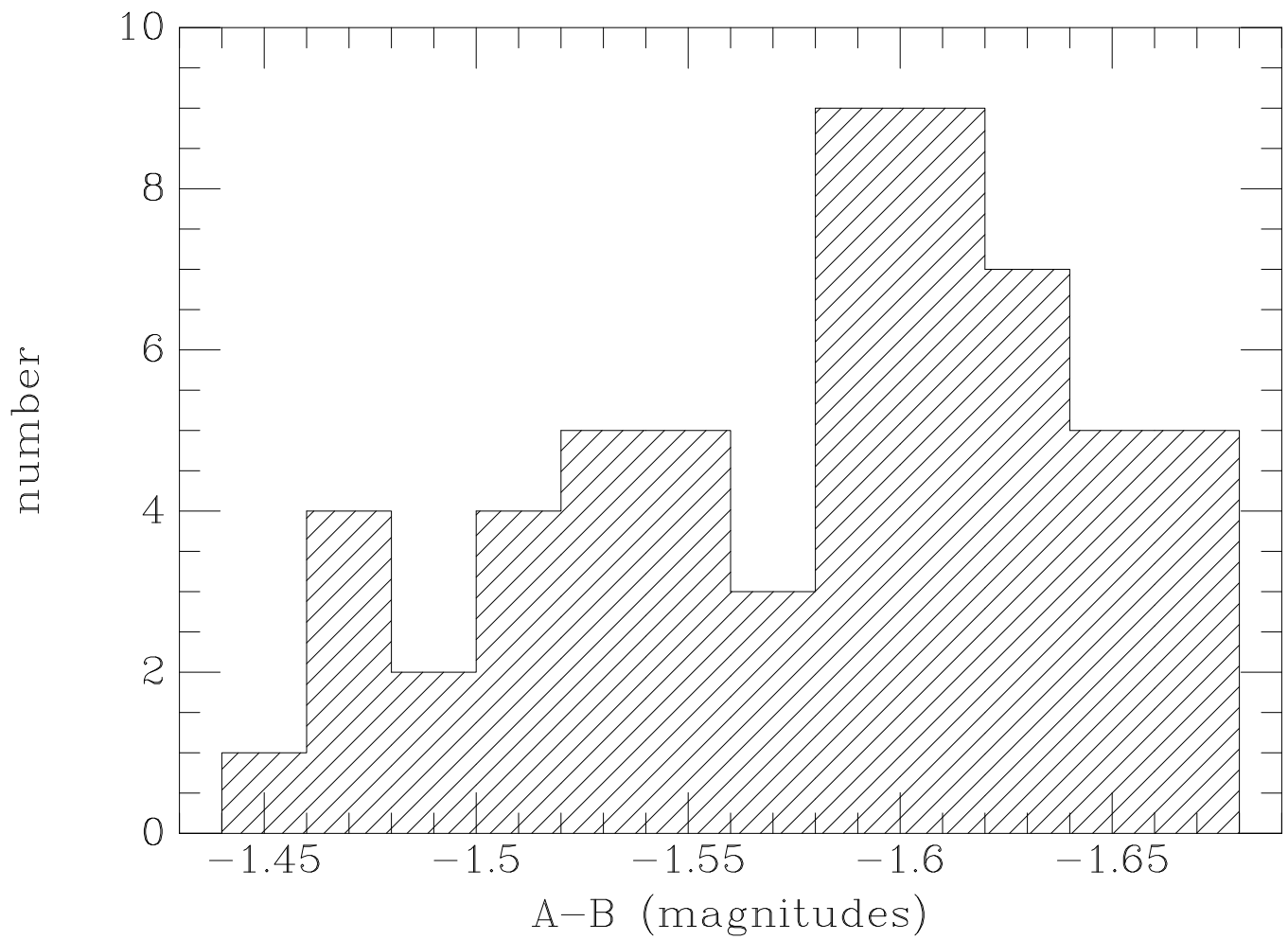


Fig. 7.— Histogram of $A - B$ magnitude differences

TABLE 1
OBSERVATIONS OF HE1104-1805 A, B AND CA

date (JD - 2445000)	m_A (mag)	m_B (mag)	m_{CA} (mag)
666.464	-1.415	0.283	-0.388
666.473	-1.415	0.277	-0.387
760.848	-1.357	0.338	-0.389
760.856	-1.351	0.327	-0.385
762.854	-1.338	0.373	-0.381
763.855	-1.354	0.357	-0.392
773.847	-1.338	0.362	-0.393
773.855	-1.341	0.354	-0.392
782.841	-1.372	0.392	-0.394
782.850	-1.375	0.365	-0.393
783.843	-1.363	0.352	-0.389
783.852	-1.375	0.362	-0.390
789.850	-1.356	0.361	-0.385
792.812	-1.389	0.380	-0.396
792.821	-1.395	0.348	-0.394
800.843	-1.405	0.385	-0.403
800.852	-1.412	0.370	-0.397
800.863	-1.388	0.405	-0.407
806.852	-1.375	0.380	-0.390
806.860	-1.387	0.369	-0.394
816.861	-1.386	0.404	-0.393
816.872	-1.402	0.381	-0.388
817.846	-1.403	0.396	-0.392
817.855	-1.395	0.402	-0.394
820.868	-1.407	0.393	-0.402
833.805	-1.386	0.428	-0.396
833.813	-1.368	0.429	-0.385
840.791	-1.386	0.402	-0.390
840.799	-1.383	0.389	-0.384
850.813	-1.324	0.378	-0.391
850.821	-1.320	0.376	-0.385
864.653	-1.359	0.381	-0.392
864.662	-1.366	0.365	-0.399
866.779	-1.370	0.370	-0.392
866.788	-1.361	0.353	-0.394
874.766	-1.351	0.389	-0.390
874.775	-1.371	0.376	-0.391
878.668	-1.391	0.389	-0.391
878.677	-1.390	0.363	-0.388
891.741	-1.346	0.430	-0.386
891.750	-1.343	0.430	-0.389
900.644	-1.312	0.439	-0.386

TABLE 1—*Continued*

date (JD − 2445000)	m_A (mag)	m_B (mag)	m_{CA} (mag)
900.652	-1.317	0.433	-0.390
909.582	-1.242	0.441	-0.388
909.590	-1.262	0.435	-0.397
911.773	-1.247	0.459	-0.376
911.782	-1.253	0.491	-0.386
917.683	-1.227	0.451	-0.379
917.691	-1.240	0.461	-0.387
921.645	-1.214	0.460	-0.391
921.654	-1.228	0.433	-0.390
928.629	-1.181	0.459	-0.382
928.638	-1.180	0.474	-0.383
936.575	-1.157	0.492	-0.388
950.574	-1.204	0.464	-0.381
950.583	-1.228	0.462	-0.396
962.521	-1.243	0.471	-0.391
962.529	-1.240	0.476	-0.387
966.549	-1.229	0.486	-0.384
971.467	-1.211	0.496	-0.401
971.477	-1.209	0.502	-0.389
971.477	-1.209	0.502	-0.389
985.494	-1.198	0.479	-0.396
985.503	-1.172	0.491	-0.388
990.486	-1.214	0.491	-0.396
990.494	-1.223	0.493	-0.390
996.469	-1.218	0.484	-0.387
996.478	-1.224	0.501	-0.396
1011.490	-1.245	0.528	-0.395
1011.499	-1.238	0.522	-0.391
1020.477	-1.256	0.528	-0.393
1020.486	-1.254	0.523	-0.387
1026.474	-1.265	0.527	-0.395
1026.483	-1.259	0.563	-0.389
1036.476	-1.191	0.533	-0.385
1036.468	-1.198	0.539	-0.384
1126.839	-1.206	0.480	-0.375
1126.848	-1.191	0.448	-0.366
1135.836	-1.242	0.479	-0.388
1135.844	-1.238	0.465	-0.382
1143.842	-1.208	0.509	-0.399
1143.850	-1.211	0.496	-0.382
1155.839	-1.169	0.477	-0.386
1155.847	-1.170	0.501	-0.375

TABLE 1—*Continued*

date (JD − 2445000)	m_A (mag)	m_B (mag)	m_{CA} (mag)
1164.815	-1.203	0.504	-0.401
1164.824	-1.206	0.493	-0.391
1174.790	-1.170	0.518	-0.389
1174.799	-1.172	0.518	-0.387
1186.811	-1.097	0.519	-0.404
1186.820	-1.105	0.506	-0.390
^a 1192.759	-0.852	0.523	-0.389
1192.768	-1.121	0.515	-0.393
1196.783	-1.096	0.545	-0.391
1196.791	-1.110	0.530	-0.388
1203.783	-1.106	0.558	-0.389
1203.792	-1.112	0.549	-0.382
1216.777	-1.182	0.540	-0.391
1216.785	-1.180	0.534	-0.391
1222.769	-1.158	0.557	-0.383
1222.777	-1.162	0.541	-0.384
1224.755	-1.147	0.554	-0.379
1224.764	-1.171	0.559	-0.396
^a 1230.785	-1.139	0.482	-0.384
1230.793	-1.147	0.547	-0.389
1246.700	-1.165	0.532	-0.391
1246.709	-1.161	0.528	-0.390
1254.746	-1.145	0.533	-0.386
1254.754	-1.141	0.535	-0.386
1262.730	-1.164	0.500	-0.391
1262.739	-1.162	0.514	-0.388
1276.591	-1.070	0.504	-0.388
1276.599	-1.065	0.513	-0.385
1281.665	-1.085	0.497	-0.398
1281.673	-1.061	0.507	-0.381
1288.625	-1.084	0.492	-0.383
1288.633	-1.093	0.477	-0.389
1294.621	-1.110	0.479	-0.398
1294.629	-1.119	0.474	-0.390
1306.602	-1.133	0.491	-0.388
1306.611	-1.152	0.473	-0.382
1316.634	-1.120	0.490	-0.388
1316.642	-1.135	0.487	-0.388
1321.636	-1.070	0.482	-0.384
1339.496	-1.057	0.501	-0.387
1339.505	-1.056	0.490	-0.390
1345.498	-1.049	0.501	-0.391

TABLE 1—*Continued*

date (JD − 2445000)	m_A (mag)	m_B (mag)	m_{CA} (mag)
1345.506	-1.053	0.511	-0.387
1352.459	-1.053	0.489	-0.390
1352.467	-1.060	0.485	-0.388
1365.471	-1.081	0.497	-0.383
1365.479	-1.084	0.476	-0.387
1373.472	-1.076	0.452	-0.390
1373.480	-1.099	0.470	-0.387
1394.488	-1.065	0.448	-0.387
1394.496	-1.054	0.454	-0.389
1398.468	-1.088	0.499	-0.396
1398.477	-1.083	0.464	-0.388
1489.848	-1.143	0.449	-0.388
1489.857	-1.156	0.452	-0.388
1497.850	-1.100	0.448	-0.389
1512.829	-1.129	0.448	-0.373
1512.838	-1.118	0.464	-0.382
1519.829	-1.133	0.455	-0.388
1519.837	-1.126	0.460	-0.386
1526.838	-1.116	0.435	-0.392
1526.846	-1.109	0.473	-0.394
1542.853	-1.134	0.504	-0.379
1544.819	-1.135	0.517	-0.388
1544.828	-1.138	0.496	-0.398
1552.838	-1.101	0.526	-0.388
1552.847	-1.103	0.514	-0.389
1562.843	-1.065	0.536	-0.387
1562.851	-1.054	0.526	-0.393
1572.817	-1.032	0.516	-0.392
1572.826	-1.030	0.527	-0.382
1581.779	-1.018	0.531	-0.387
1581.787	-1.020	0.507	-0.377
1588.770	-1.010	0.545	-0.395
1588.782	-1.003	0.541	-0.393
1601.780	-1.118	0.538	-0.387
1601.788	-1.115	0.518	-0.391
1608.769	-1.119	0.528	-0.385
1608.778	-1.126	0.535	-0.385
1616.752	-1.129	0.519	-0.390
1616.760	-1.135	0.531	-0.385
1629.673	-1.142	0.533	-0.386
1629.682	-1.160	0.527	-0.392
1634.668	-1.170	0.520	-0.393

TABLE 1—*Continued*

date (JD – 2445000)	m_A (mag)	m_B (mag)	m_{CA} (mag)
1634.677	-1.156	0.541	-0.389
1643.640	-1.096	0.495	-0.387
1643.649	-1.130	0.493	-0.394
1646.583	-1.108	0.506	-0.385
1646.591	-1.110	0.477	-0.393
1659.625	-1.037	0.526	-0.376
1659.634	-1.052	0.511	-0.388
1667.599	-1.049	0.512	-0.375
1667.607	-1.049	0.510	-0.387
1675.566	-1.070	0.481	-0.388
1675.575	-1.080	0.501	-0.389
1687.534	-1.088	0.522	-0.387
1687.542	-1.082	0.529	-0.383
1698.517	-1.033	0.538	-0.383
1698.525	-1.035	0.549	-0.381
1705.539	-1.001	0.567	-0.389
1705.547	-1.009	0.548	-0.392
1717.464	-1.000	0.574	-0.390
1717.483	-1.000	0.571	-0.384
1717.491	-0.999	0.592	-0.374
1729.488	-1.018	0.600	-0.387
1729.496	-1.010	0.623	-0.387
1738.481	-1.026	0.610	-0.400
1738.489	-1.018	0.636	-0.393
1748.489	-1.013	0.636	-0.388
1753.476	-0.972	0.645	-0.391
1753.484	-0.969	0.647	-0.378
^a 1759.454	-1.005	0.565	-0.388
1759.463	-0.989	0.658	-0.393

^aObservation discarded

TABLE 2
LENSING PARAMETERS FOR IMAGES A AND B

Image	κ_{tot}	γ	μ
A	0.639	0.521	-7.08
B	0.335	0.215	+2.53